NANOMATERIALS

10.1126/sciadv.1500259

Hierarchical Ni-Mo-S nanosheets on carbon fiber cloth: A flexible electrode for efficient hydrogen generation in neutral electrolyte

Jianwei Miao,[1] Fang-Xing Xiao,[1] Hong Bin Yang,[1] Si Yun Khoo,[1] Jiazang Chen,[1] Zhanxi Fan,[2] Ying-Ya Hsu,[3] Hao Ming Chen,[3] Hua Zhang,[2]* Bin Liu[1]*

A unique functional electrode made of hierarchal Ni-Mo-S nanosheets with abundant exposed edges anchored on conductive and flexible carbon fiber cloth, referred to as Ni-Mo-S/C, has been developed through a facile biomolecule-assisted hydrothermal method. The incorporation of Ni atoms in Mo-S plays a crucial role in tuning its intrinsic catalytic property by creating substantial defect sites as well as modifying the morphology of Ni-Mo-S network at atomic scale, resulting in an impressive enhancement in the catalytic activity. The Ni-Mo-S/C electrode exhibits a large cathodic current and a low onset potential for hydrogen evolution reaction in neutral electrolyte (pH ~7), for example, current density of 10 mA/cm^2 at a very small overpotential of 200 mV. Furthermore, the Ni-Mo-S/C electrode has excellent electrocatalytic stability over an extended period, much better than those of MoS_2/C and Pt plate electrodes. Scanning and transmission electron microscopy, Raman spectroscopy, x-ray diffraction, x-ray photoelectron spectroscopy, and x-ray absorption spectroscopy were used to understand the formation process and electrocatalytic properties of Ni-Mo-S/C. The intuitive comparison test was designed to reveal the superior gas-evolving profile of Ni-Mo-S/C over that of MoS_2/C, and a laboratory-scale hydrogen generator was further assembled to demonstrate its potential application in practical appliances.

INTRODUCTION

On the journey to pursue clean and sustainable energy resources, electrocatalytic and photoelectrocatalytic water splitting have attracted growing attention because of their potential applications in producing hydrogen with ultrahigh purity while generating negligible greenhouse gases (*1*, *2*). Hydrogen evolution reaction (HER), in which protons are reduced to molecular hydrogen, is a critical process for electrocatalytic water splitting (*2*). Although platinum (Pt) is the most effective HER electrocatalyst, the scarcity and expensiveness limit its practical applications for large-amount hydrogen generation (*3*, *4*). Therefore, exploration of alternative earth-abundant materials with low cost and high catalytic activity is essential for developing a high-performance electrocatalyst toward large-amount hydrogen production.

MoS_2, a layered transition metal dichalcogenide, has been shown as a versatile functional material for various applications (*5*–*7*), including lithium-ion batteries (*8*–*10*), nanoelectronics (*11*, *12*), hydrodesulfurization (*13*), and HER catalysts (*14*). The earliest observation of hydrogen evolution on MoS_2 can be dated back to more than 40 years ago (*15*). Later, in 1991, Sobczynski reported MoS_2 as an HER cocatalyst for water photodecomposition on semiconductors (*16*). Since then, MoS_2-based catalysts have been thoroughly studied and widely recognized as ideal catalysts for hydrogen generation in acidic medium (*17*). More recently, a number of computational and experimental studies suggest that the HER activities of nano-sized MoS_2 particles originate from the edge sites while their basal planes are catalytically inactive (*18*). To fully exploit the advantageous catalytic properties, well-defined MoS_2 nanostructures with abundant exposed catalytic active sites and enhanced intrinsic properties should be rationally designed. Various strategies have been proposed and reported for improving the catalytic activity of MoS_2-based HER catalysts. For example, Li *et al.* reported the synthesis of MoS_2 nanoparticles anchored on graphene through a solvothermal approach. The composite catalyst showed superior catalytic performance owing to the abundant exposed edges as well as the strong chemical and electronic coupling between graphene oxide (GO) and MoS_2 (*19*). Kibsgaard *et al.* successfully engineered MoS_2 into highly ordered, double-gyroid network, in which active edge sites in MoS_2 are preferentially exposed for electrocatalysis (*20*). Recently, Wang *et al.* showed the preparation of vertically aligned MoS_2 nanofilms with improved HER activity by electrochemical lithium intercalation (*21*). Lu *et al.* demonstrated that the aerophobic surface of nanostructured MoS_2 is more beneficial for releasing gas bubbles during HER as compared to the planar thin film (*22*). Besides the aforementioned design and construction of nanostructures, controllable disorder engineering is another approach that can be used to improve the catalytic activities of MoS_2. For example, Xie *et al.* reported the syntheses of defect-rich MoS_2 ultrathin nanosheets through controlling experimental conditions such as precursor concentration and reaction temperature (*23*, *24*). They discovered that the introduction of defect sites could lead to the exposure of additional catalytic centers, thus significantly improving the catalytic performance of MoS_2.

All of the aforementioned strategies are important and provide us valuable guidelines to further excavate the potential of MoS_2-based electrocatalysts. However, most of the current studies on MoS_2-based electrocatalysts are only viable for laboratory-scale applications under ideal experimental conditions, and are not ready to be applied in practical industrial appliances. For the purpose of developing qualified H_2 gas–evolving electrodes that can be integrated in large-scale reactors, the following criteria have to be fulfilled. First, the attached HER catalyst must exhibit extraordinary catalytic activity and reasonable stability for long-term operation. Second, the catalysts and their supporting materials should be abundant and cost-effective and able to be mass-produced.

---

[1]School of Chemical and Biomedical Engineering, Nanyang Technological University, Singapore 637459, Singapore. [2]School of Materials Science and Engineering, Nanyang Technological University, Singapore 639798, Singapore. [3]Department of Chemistry, National Taiwan University, Taipei 106, Taiwan.
*Corresponding author. E-mail: liubin@ntu.edu.sg (B.L.); hzhang@ntu.edu.sg (H.Z.)

Third, the catalysts, substrates, and operating environment have to be nontoxic and eco-friendly, in accordance with the intention of developing sustainable energy resources. Last, the electrodes should have excellent mechanical strength and physical flexibility, which allow them to be integrated in varied reactors to meet different requirements and standards. Thanks to the rapid development in the theoretical calculation as well as experimental techniques, the progress of developing gas-evolving electrodes for practical applications has been significantly accelerated over the past few years (*25*–*28*).

Herein, we report a facile synthetic strategy to directly grow nanostructured Ni-Mo-S on three-dimensional (3D) flexible and conductive carbon fiber cloth substrate. We found that the introduction of nickel ion (Ni^{2+}) in the precursor solution played a crucial role in tailoring the morphology and intrinsic properties of MoS_2, hence effectively affecting their catalytic behaviors. The optimized Ni-Mo-S/C electrode showed pronounced HER electrocatalytic activity in neutral electrolyte with remarkable stability. The as-synthesized Ni-Mo-S catalysts were characterized by scanning and transmission electron microscopies (SEM and TEM), Raman spectroscopy, x-ray diffraction (XRD), x-ray photoelectron spectroscopy (XPS), and x-ray absorption spectroscopy. A prototype of a laboratory-scale H_2 generator was designed to show the applicability of the Ni-Mo-S/C electrode for future large-scale applications.

RESULTS

Here, our first attempt was to synthesize nanostructured MoS_2 onto various carbon-based substrates, including carbon fiber cloth (fig. S1) and graphite foil, which can be directly used as functional electrodes for hydrogen evolution. In these experiments, a biomolecule-assisted hydrothermal synthetic route with $Na_2MoO_4 \cdot 2H_2O$ and L-cysteine (L-Cys) as the Mo and S sources, respectively, was used to synthesize nanostructured MoS_2. As one type of amino acid, the L-Cys molecules can be assembled into a polymeric network structure through the formation of peptide bonds and disulfide bonds from the dehydration condensation and sulfhydryl (-SH) group oxidation reactions. The as-formed 3D network is beneficial for the construction of nanostructured materials. Upon heating to a certain temperature, L-Cys starts to decompose and releases H_2S that is capable of reducing MoO_4^{2-} to MoS_2 on the basis of the following reactions (*8*, *29*):

$$\mathrm{HSCH_2CHNH_2COOH + H_2O \rightarrow CH_3COCOOH + NH_3 + H_2S}$$

$$\mathrm{4MoO_4^{2-} + 9H_2S + 6CH_3COCOOH \rightarrow 4MoS_2 + SO_4^{2-} + 6CH_3COCOO^- + 12\ H_2O}$$

However, it was found that MoS_2 nanostructures prepared by this method could easily coalesce and stack together to form bulky and non-uniform aggregates on carbon fibers. The coalescence and stacking of nanostructures are detrimental for MoS_2-based electrocatalysts because aggregation leads to a drastic decrease in numbers of exposed active sites along the edges. The aggregation is attributed to the epitaxial nucleation and growth of layered MoS_2, which is further elaborated in the Supplementary Materials (figs. S2 and S3 and note S1).

To tailor the morphologies and intrinsic properties of MoS_2 on carbon fibers, the synthetic strategy was modified by introducing Ni^{2+} into the precursor solution. As shown in Fig. 1A, MoS_2 and Ni-Mo-S samples with different Ni-to-Mo precursor ratios, namely, 3:1, 1:1, and 1:3, were directly synthesized on carbon fiber cloth, designated as MoS_2/C and Ni-Mo-S/C (3:1), Ni-Mo-S/C (1:1), and Ni-Mo-S/C (1:3), respectively. For comparison purpose, NiS_x/C was also synthesized using a similar hydrothermal approach. Figure 1B shows a photographic image of a freshly synthesized Ni-Mo-S/C (1:1) with a dimension of 5 × 3 cm.

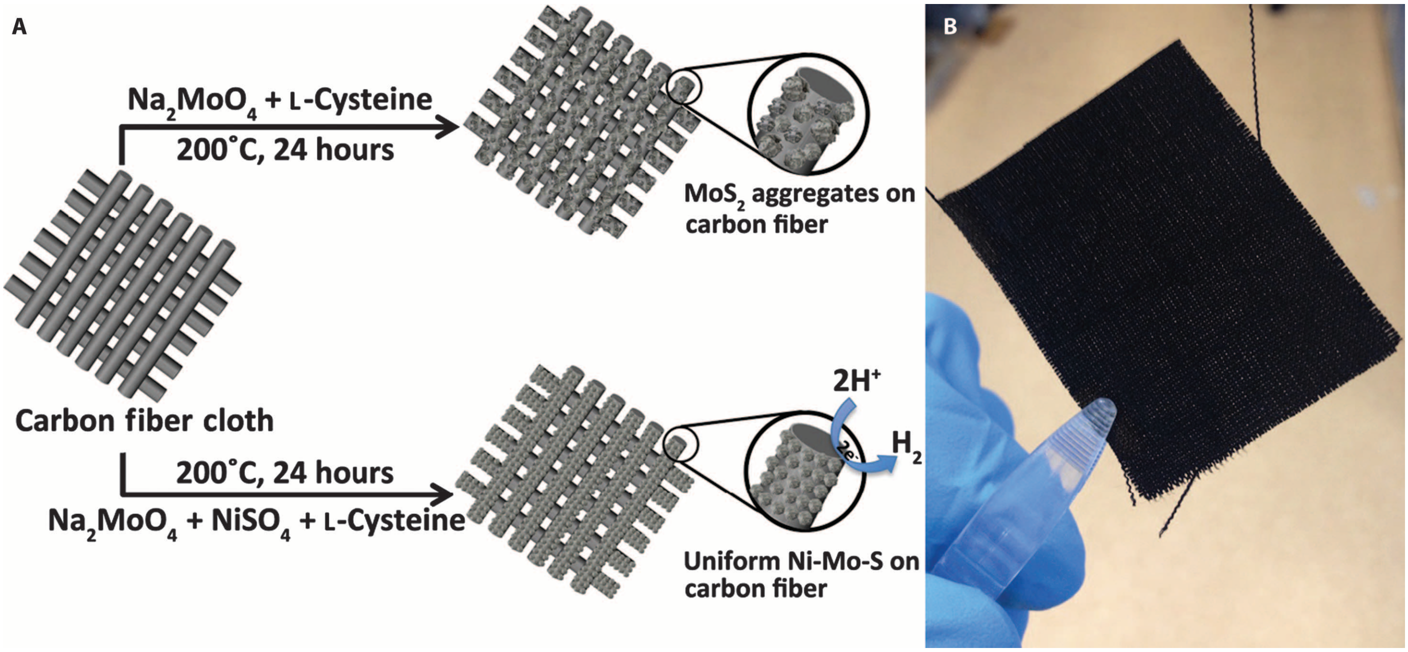

Fig. 1. Synthesis processes of MoS_2/C and Ni-Mo-S/C. (**A**) Schematic illustration of syntheses of MoS_2 and Ni-Mo-S on carbon fiber cloth. (**B**) Photographic image of freshly prepared Ni-Mo-S/C (1:1).

Figure 2 shows the typical low-magnification SEM images of bare carbon fiber from the cloth, NiS_x/C, Ni-Mo-S/C, and MoS_2/C. As displayed in Fig. 2A, the diameter of a single carbon fiber is ~10 μm. Oriented striations that formed during the manufacturing process are along the entire surface of fibers. Figure 2B shows the morphology of as-prepared NiS_x/C, where the irregularly shaped NiS_x particles with sizes ranging from 100 nm to 1 μm form a shell-like outer layer that covers the carbon fiber surface. However, the NiS_x particles are loosely attached to the surface of carbon fibers with clear cracks formed between them (fig. S4). The introduction of Ni^{2+} in the precursor solution plays a critical role in tuning the nanoarchitectures of Ni-Mo-S/C. At a Ni-to-Mo precursor ratio of 3:1, the surface of carbon fibers was first covered with a rough and tight nanostructured film, followed by attachment of particles with random shape and size (Fig. 2C). The nanostructured film, which shows clear visible striations, is thinner as compared to NiS_x/C. When the Ni-to-Mo precursor ratio is reduced to 1:1, a uniform and continuous nanostructured film could be grown on the entire surfaces of carbon fibers (Fig. 2D). However, further increase in the Mo content (Ni/Mo = 1:3) in the growth solution leads to the formation of large aggregates (Fig. 2E). Moreover, if no Ni^{2+} was added in the growth solution, non-uniform MoS_2 aggregates would cover the entire surface of carbon fibers.

To gain more detailed insights into the morphological evolution, we further compared the high-magnification SEM images of different Ni-Mo-S/C samples. Figure 3A reveals that the nanostructured film in Ni-Mo-S/C (3:1) is composed of numerous nanosheets and large aggregated nanoparticles, which tightly stack onto the surface of carbon fibers. When the Ni-to-Mo ratio in the precursor solution is reduced to 1:1, a uniform nanostructured film composed of abundant edge-exposing nanosheets with an average thickness of 8 to 10 nm is formed, which develops into a nanoscale 3D network (Fig. 3B). The 3D nanostructure of Ni-Mo-S/C (1:1) is expected to benefit its HER application (*22*). Further increase in the Mo content in the growth solution (Ni/Mo, 1:3) results in the formation of bulky aggregates, which significantly decreases the density of exposed edge structures (Fig. 3C). If no Ni^{2+} is introduced into the synthesis, freely grown MoS_2 can easily form large aggregates, which folded together and resembled the morphology of crumpled paper balls (Fig. 3D). The average thickness of MoS_2 nanosheets is about 20 to 30 nm, which is about three times thicker than the edges in Ni-Mo-S (1:1) (Fig. 3B). The morphologies of different aggregates in different samples were compared (see fig. S5). It was found that the aggregates in MoS_2/C, Ni-Mo-S/C (1:3), and Ni-Mo-S/C (1:1) are morphologically similar, and are all evolved from crumpled 2D-layered structures. In contrast, although the aggregates in Ni-Mo-S/C (3:1) and NiS_x are similar in appearance, both of the aggregates are formed from nanoparticles. Obviously, the introduction of Ni^{2+} during the synthesis plays important roles in regulating the development of Ni-Mo-S nanostructures. The added Ni^{2+} may suppress the MoS_2 crystal growth along the basal planes, thus lowering the probability of formation of stack-ups and coalescences among the nanosheets. However, overwhelming Ni^{2+} will prevent the formation of preferable 3D nanostructures on carbon fibers. Therefore, the optimized Ni-to-Mo precursor ratio in our synthesis is 1:1.

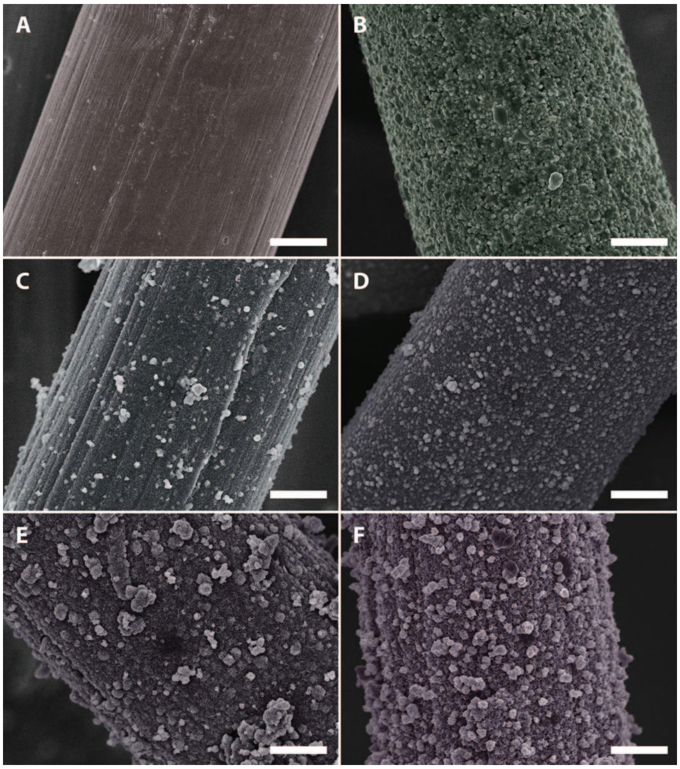

Fig. 2. Low-magnification SEM images. (**A**) Bare carbon fiber cloth. (**B**) NiS_x/C. (**C**) Ni-Mo-S/C (3:1). (**D**) Ni-Mo-S/C (1:1). (**E**) Ni-Mo-S/C (1:3). (**F**) MoS_2/C. All scale bars, 2 μm.

Energy-dispersive x-ray spectroscopy (EDS) measurements were performed to study the elemental composition of the samples (fig. S6). The spectrum of MoS_2/C affirms that the atomic ratio of Mo/S is close to 1:2, which is consistent with the stoichiometric ratio of MoS_2. However, the measured Ni-to-Mo ratios in Ni-Mo-S/C (3:1), Ni-Mo-S/C (1:1), and Ni-Mo-S/C (1:3) are 1:4.5, 1:8.3, and 1:11.3, respectively, which differ from their corresponding precursor ratios. On the basis of these observations, we believe that the predominant constituents in all Ni-Mo-S/C samples should be Ni-incorporated MoS_x. Point EDS was performed to further confirm the composition of aggregates in Ni-Mo-S/C (3:1). As shown in fig. S7, it is observed that the ratio of Ni/Mo on the aggregate is ~1.61:1, significantly higher than the nonaggregated area (~0.47:1). It suggests that the aggregates in Ni-Mo-S/C (3:1) are Ni-rich, most probably due to the presence of NiS_x nanoparticles that were adsorbed onto the electrode surface.

To better elucidate the morphological distinction between Ni-Mo-S/C (1:1) and MoS_2/C, TEM images were carried out. Figure 4 (A and B) shows TEM images of MoS_2/C and Ni-Mo-S/C (1:1). MoS_2 has continuous and corrugated layered structures, where restacked and wrinkled parts can be clearly observed. In contrast, the introduction of Ni^{2+} during the synthesis leads to the formation of interconnected Ni-Mo-S flake-like structures. In the high-resolution TEM (HRTEM) images (Fig. 4, C and D), lattices with a spacing of 0.27 nm, which can be assigned to the (100) plane of 2H-MoS_2, are identified in both samples. However, as compared to MoS_2/C, the crystalline quality of Ni-Mo-S/C was significantly reduced. As indicated by dashed circles in Fig. 4D, numerous structure defects can be observed in the surface of nanoflakes (see fig. S8). The insets in Fig. 4 (C and D) show the cross-sectional views of stacked MoS_2/C and Ni-Mo-S/C (1:1), respectively. We found that the (002) plane spacing of Ni-Mo-S/C (1:1), which correlates to the interlayer distance, is significantly enlarged to 0.92 nm from 0.63 nm observed in MoS_2/C. To assess the distribution of Ni across the basal plane of Ni-Mo-S/C (1:1), EDS mapping was performed. As shown in fig. S9, both Mo and S are uniformly distributed in the entire detected region. Meanwhile, the distribution of incorporated Ni atoms on the structure is quite homogeneous, although its concentration is slightly higher near the defect-rich regions.

Porosity is another important property for electrocatalysts because porous structures could provide channels that allow fast access to electrolytes and efficient transport of reactants and products. The nitrogen adsorption/desorption analyses were conducted to analyze the porosity of the as-synthesized Ni-Mo-S/C (1:1) as shown in fig. S10. The curve shows typical type IV isotherm hysteresis according to International Union of Pure and Applied Chemistry classification (*30*), affirming the mesoporous structure of Ni-Mo-S/C (1:1). As indicated by the inset of fig. S10, the size of most pores formed on Ni-Mo-S/C (1:1) falls in the range of 2 to 10 nm. This conclusion is consistent with our observation in TEM (Fig. 4 and fig. S8), in which the pores, due to the defect formation, can be clearly observed on the basal plane of Ni-Mo-S/C (1:1). Apart from the mesopores, numerous macropores ranging from 50 to 100 nm can also be formed among the adjacent nanosheets in the structure. However, these macropores could not be precisely detected using the Brunauer-Emmett-Teller (BET) method. The porous nature of Ni-Mo-S/C (1:1) should significantly benefit the electrocatalytic hydrogen evolution process.

To understand the crystal structure of Ni-Mo-S/C samples, XRD patterns were studied in detail. Because the XRD pattern of Ni-Mo-S/C (1:1) shows a predominant diffraction peak at 26° that can be indexed to the (002) plane of carbon (inset of Fig. 5), the XRD pattern of Ni-Mo-S (1:1) was precisely extracted using Bruker EVA software by subtraction of the signal from carbon fiber cloth (Fig. 5). The broadened diffraction peaks imply the nanoscale dimensions of Ni-Mo-S flakes on the carbon fiber cloth. Compared to the reference XRD pattern (Joint Committee on Powder Diffraction Standards card no. 73-1508), the (002) peak of pristine 2H-MoS_2 at 14.39° is absent in the Ni-Mo-S/C (1:1) sample. Instead, two new diffraction peaks at 9.22° and 17.64° can

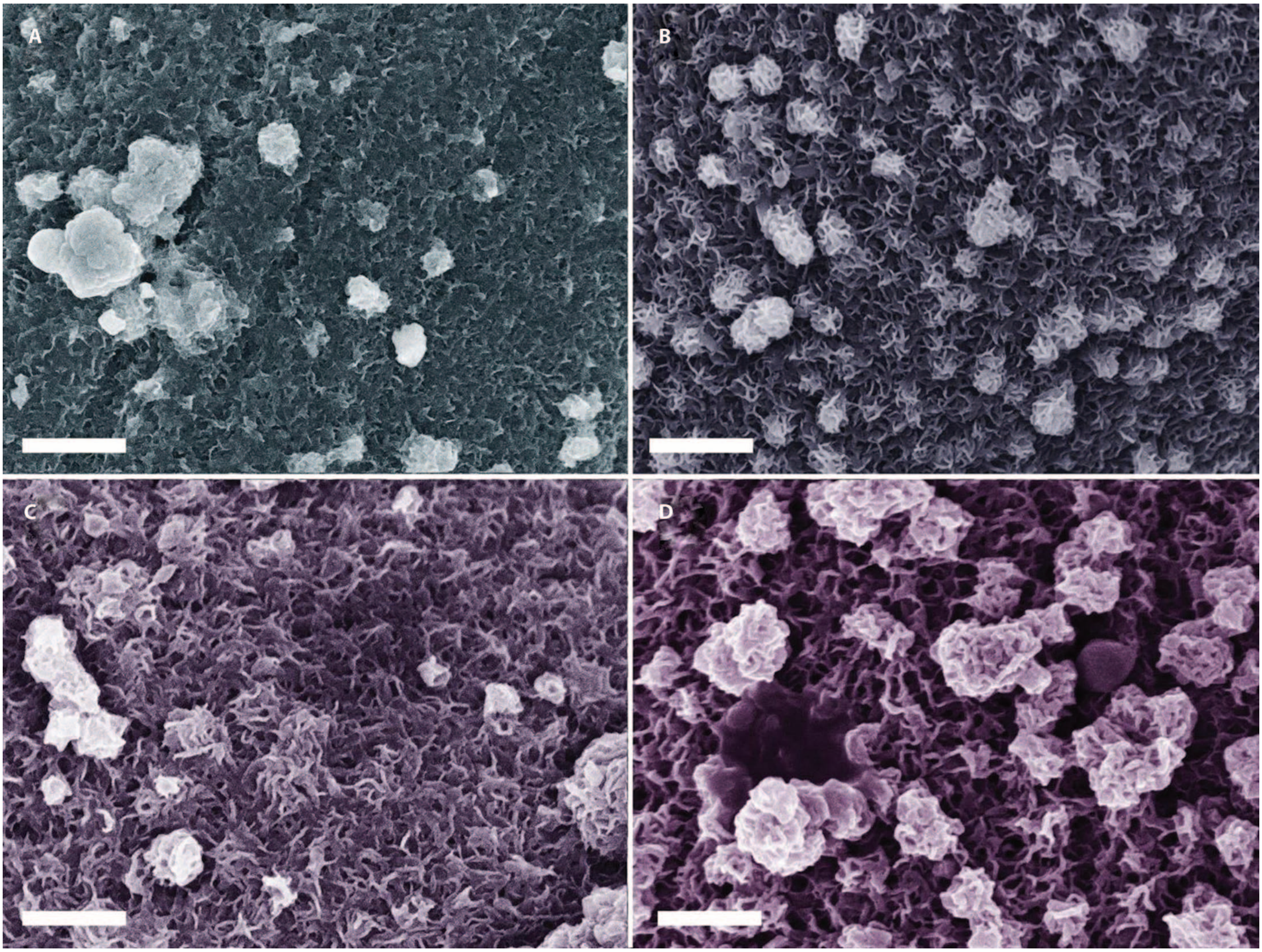

Fig. 3. High-magnification SEM images. (**A**) Ni-Mo-S/C (3:1). (**B**) Ni-Mo-S/C (1:1). (**C**) Ni-Mo-S/C (1:3). (**D**) MoS_2/C. All scale bars, 500 nm.

be observed, which most probably correspond to the first- and second-order reflections from the (002) plane of layered Ni-Mo-S, respectively. Our observation is similar to the MoS_2 nanosheets with enlarged interlayer spacing that was recently reported by Xie *et al.* (*24*). In this case, the spacing between two adjacent Ni-Mo-S layers can be calculated using Bragg's law (*31*):

$$n\lambda = 2d\sin\theta,$$

where n is the order of reflection, λ is the wavelength of incident x-ray (Cu Kα, 0.154 nm), d is the interlayer spacing, and θ is the angle between the incident x-ray and the scattering planes. The calculated spacing between Ni-Mo-S layers is about 0.94 to 0.95 nm, consistent with our observations in HRTEM images (0.92 nm in inset of Fig. 4D). Moreover, two diffraction peaks centered at 32° and 57° can be well indexed to the (100) and (110) planes of 2H-MoS_2, showing that the atomic arrangement of Ni-Mo-S (1:1) should be similar to that of pristine MoS_2. In addition, the asymmetric features of these two peaks reflect the turbostratic stacking characteristic of Ni-Mo-S flakes, which is commonly observed in other layered compounds (*32*). The absence of other high-angle diffraction peaks suggests the structure-disordering feature of Ni-Mo-S because of the presence of abundant defect sites across its basal planes. It is worth mentioning that diffraction peaks that correlate to nickel sulfide and its nonstoichiometric forms were absent in the XRD pattern of Ni-Mo-S/C (1:1).

Figure 6 shows the Raman spectra of Ni-Mo-S/C (1:1) and MoS_2/C. Two distinct peaks at ~380 and ~405 cm^{-1}, corresponding to the in-plane E^1_{2g} and out-of-plane A_{1g} vibrational modes of 2H-MoS_2, can be clearly identified in the spectra of both MoS_2/C and Ni-Mo-S/C (1:1) (*20*, *33*, *34*). The slightly red shift and broadening of the A_{1g} peak in Ni-Mo-S/C (1:1) can be attributed to reduced numbers of stacked layers along the c axis (*33*). Besides, the increased width along with reduced intensity of the E^1_{2g} peak in Ni-Mo-S/C (1:1) reveals the presence of in-plane defect sites (*35*), which is consistent with our aforementioned experimental observations (Figs. 3 and 4).

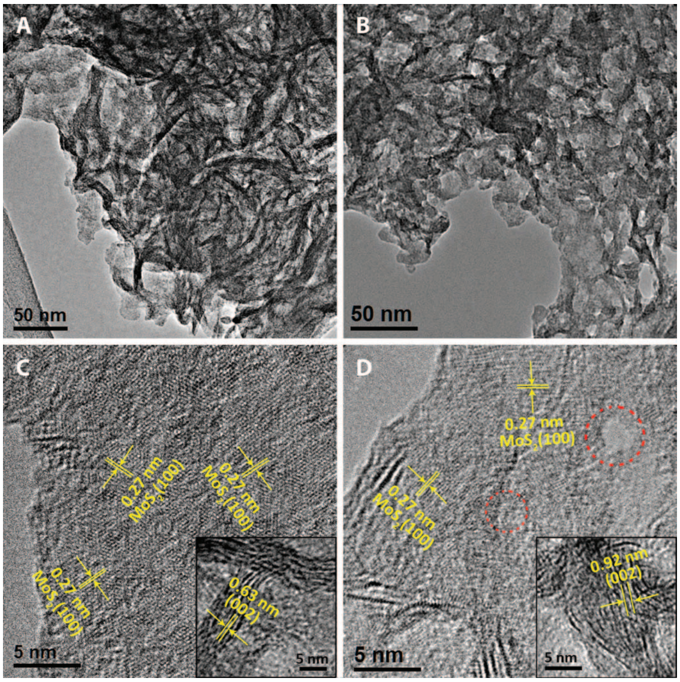

Fig. 4. TEM images. (**A** and **B**) Low-magnification TEM images of (A) MoS_2/C and (B) Ni-Mo-S/C (1:1). (**C** and **D**) HRTEM images of (C) MoS_2/C and (D) Ni-Mo-S/C (1:1). Insets: Corresponding cross-sectional HRTEM images. Dashed circles in (D) indicate the structure defects of Ni-Mo-S/C (1:1).

To further confirm the chemical composition and elemental chemical states of Ni-Mo-S/C (1:1), XPS measurements were carried out. As shown in Fig. 7A, the survey spectrum recorded from 0 to 1200 eV reveals the presence of Mo, Ni, S, C, and O elements. From the high-resolution XPS spectrum of the Mo 3*d* scan (Fig. 7B), two major peaks at 228.9 and 232 eV are observed and can be assigned to the Mo^{IV} $3d_{5/2}$ and Mo^{IV} $3d_{3/2}$ in MoS_2, affirming the dominance of $Mo^{(IV)}$ in Ni-Mo-S/C (*20*). Besides the Mo^{IV} $3d_{5/2}$ signal, there exists a small peak at 266.2 eV that resulted from the S 2*s* orbital. Another doublet at relatively higher binding energy (Mo $3d_{5/2}$, 233.1 eV; Mo $3d_{3/2}$, 235.9 eV) can be assigned to the Mo ions in the +6 oxidation state, which may be due to the inadequate reduction of MoO_4^{2-} species during the hydrothermal synthesis. The high-resolution S 2*p* spectrum clearly shows a doublet with the S $2p_{3/2}$ falling on 161.9 eV (Fig. 7C), revealing the −2 oxidation state of sulfur in MoS_2, which is consistent with previous reports (*20*, *24*). The appearance of a shoulder at higher binding energies in the S 2*p* region can serve as further evidence for the presence of Mo with higher oxidation states. As shown in Fig. 7D, the intensity of the Ni spectrum is much lower than that of other elements, due to its lower content in Ni-Mo-S/C. The calculated Ni-to-Mo ratio is about 1:8.56, which matches well with the estimated value from EDS measurements (fig. S6). The Ni spectrum shows a major peak and a satellite peak at 854.3 and 861 eV, respectively, attributed to Ni $2p_{3/2}$ orbital, which are close to the previously reported values of sulfide Ni-Mo alloys (*36*).

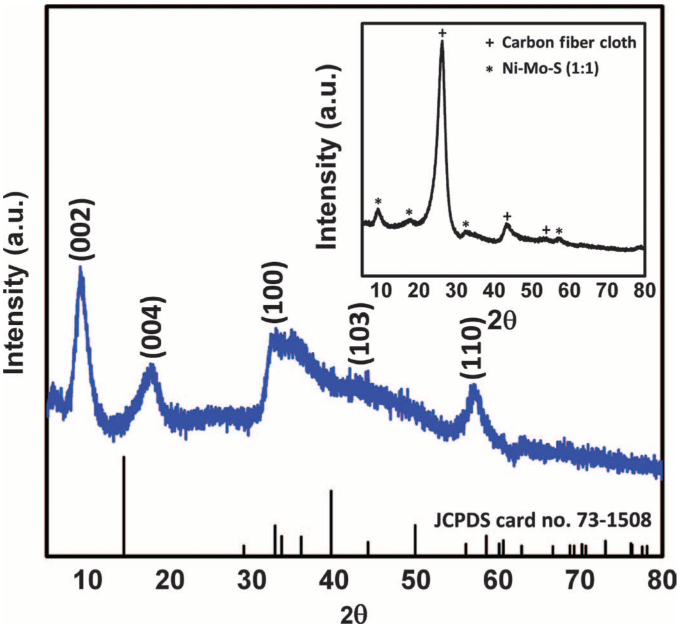

Fig. 5. XRD analysis. XRD pattern of Ni-Mo-S/C (1:1) after subtraction of carbon fiber cloth signal. Inset: Original XRD pattern of Ni-Mo-S/C (1:1). a.u., arbitrary unit.

To investigate the role of incorporated Ni on the catalytic activity of Ni-Mo-S, electrochemical measurements were designed and carried out. It is important to mention that all as-fabricated materials were directly used as working electrodes for HER without annealing or calcination. Neutral phosphate buffer solution, which could minimize the adverse environmental impacts in practical applications (*37*), was chosen as the primary electrolyte in this work. All electrochemical tests were carried out using the same setup, with consistent cell configuration, electrode positions, and electrolyte volume. The HER activities of different electrodes were investigated by comparing the polarization curves obtained with linear sweep voltammetry (LSV). In each measurement, the voltage applied on working electrode was linearly swept from 0.2 to −0.5 V versus reversible hydrogen electrode (RHE) at a scan rate of 5 mV/s. As shown in Fig. 8A, all Ni-Mo-S/C electrodes have typical onset overpotentials of 130 to 150 mV, which are apparently smaller than that of MoS_2/C (~200 mV), whereas the bare carbon fiber cloth electrode shows negligible HER catalytic activity. Among all studied samples, Ni-Mo-S/C (1:1) shows the best HER catalytic activity with a considerably smaller η_{10} (overpotential at 10 mA/cm^2) of 200 mV. At an applied potential of −0.35 V versus RHE, Ni-Mo-S/C (1:1) can produce a cathodic current density as large as 36.5 mA/cm^2, which is two times that produced by MoS_2/C. During the test, a tremendous amount of H_2 bubbles was observed on the surface of Ni-Mo-S/C (1:1) (movie S1). To ensure a fair comparison, we have normalized the performance of different electrodes (except for the blank carbon fiber cloth) by their corresponding actual catalyst loadings (Table 1) as shown in fig. S11 and found that the Ni-Mo-S/C (1:1) still shows the best performance among the samples.

To better understand the different catalytic behaviors of these electrodes, their corresponding Tafel plots were obtained from the slow-scan rate (1 mV/s) polarization curves. As shown in Fig. 8B, various Tafel slopes, ranging from 85.3 to 107.2 mV/dec, were found on different electrodes. These values are apparently larger than those recently reported for MoS_2-based electrocatalysts in acidic electrolytes (39 to 65 mV/dec) (*18*, *23*, *24*, *38*) but are comparable with those values reported using neutral electrolytes (*37*, *39*, *40*). The increase in Tafel slopes is due to the much lower proton concentration (~1×10^{-7} M, standard conditions) in neutral electrolytes than in acidic solutions, in which electrochemical hydrogen adsorption (Volmer reaction) and electrochemical desorption (Heyrovsky reaction) processes proceed at comparable rates (*39*). Although it is not possible to precisely determine the rate-determining step and exact reaction mechanism in this case, Tafel slopes of different electrodes are still important indicators for comparative analyses. Among all tested electrodes, Ni-Mo-S/C (1:1) exhibits the smallest Tafel slope (~85.3 mV/dec), which correlates well with its remarkable HER catalytic behavior originating from the abundant exposed edge sites and excellent material uniformity. In addition, the defect sites found in the basal plane of Ni-Mo-S/C (1:1) could also provide substantial extra active sites that can further enhance its HER performance. The slightly steeper Tafel slopes observed on MoS_2/C (94.4 mV/dec) and Ni-Mo-S/C (1:3) (88.4 mV/dec) may possibly be due to the formation of bulky aggregates, which, in turn, hinders the interactions between protons and effective active sites to a certain extent. As compared to MoS_2/C and other Ni-Mo-S/C samples, most probably resulting from their relatively poorer intrinsic catalytic activities, the Ni-Mo-S/C (3:1) and NiS_x/C showed much higher Tafel slopes, which are ~103.7 and ~107.2 mV/dec, respectively. Table S1 listed the exchange current densities (j_0) of different samples calculated using the Tafel equation. Ni-Mo-S/C (1:1) showed the largest j_0 among the tested electrodes, which is 4.89×10^{-2} mA/cm^2. The j_0 values of other samples follow the order of Ni-Mo-S/C (3:1) > NiS_x > Ni-Mo-S/C (1:3) > MoS_2.

For comparison purposes, electrochemical tests were also carried out in acidic electrolyte, as illustrated in fig. S12, and exhibit a similar general trend to that observed in neutral electrolyte (Fig. 8A), in which

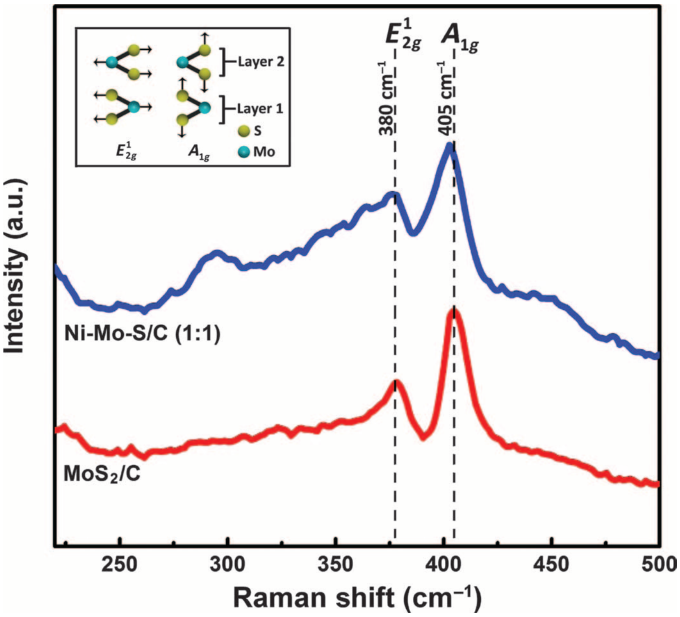

Fig. 6. Raman spectroscopy. Raman spectra of Ni-Mo-S/C (1:1) and MoS_2/C. Inset: Schematic illustration of E^1_{2g} and A_{1g} vibrational modes in layered 2H-MoS_2.

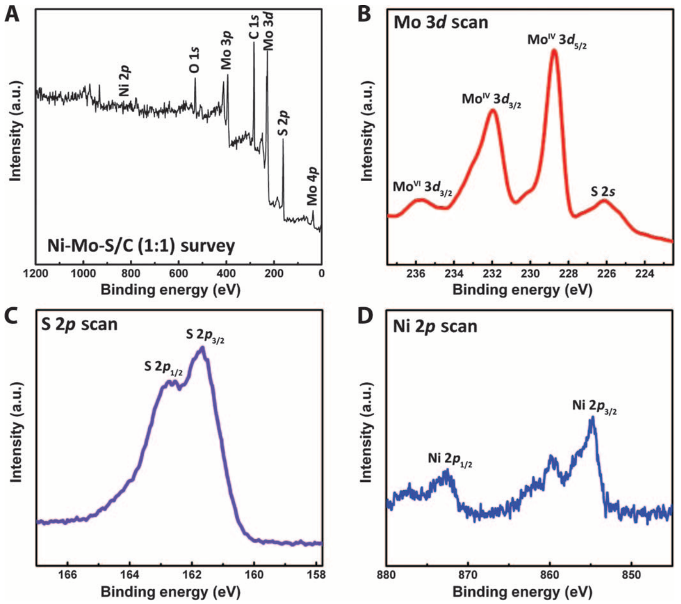

Fig. 7. XPS. (**A**) Survey XPS spectrum of Ni-Mo-S/C (1:1). (**B** to **D**) High-resolution scans of (B) Mo 3*d*, (C) S 2*p*, and (D) Ni 2*p*.

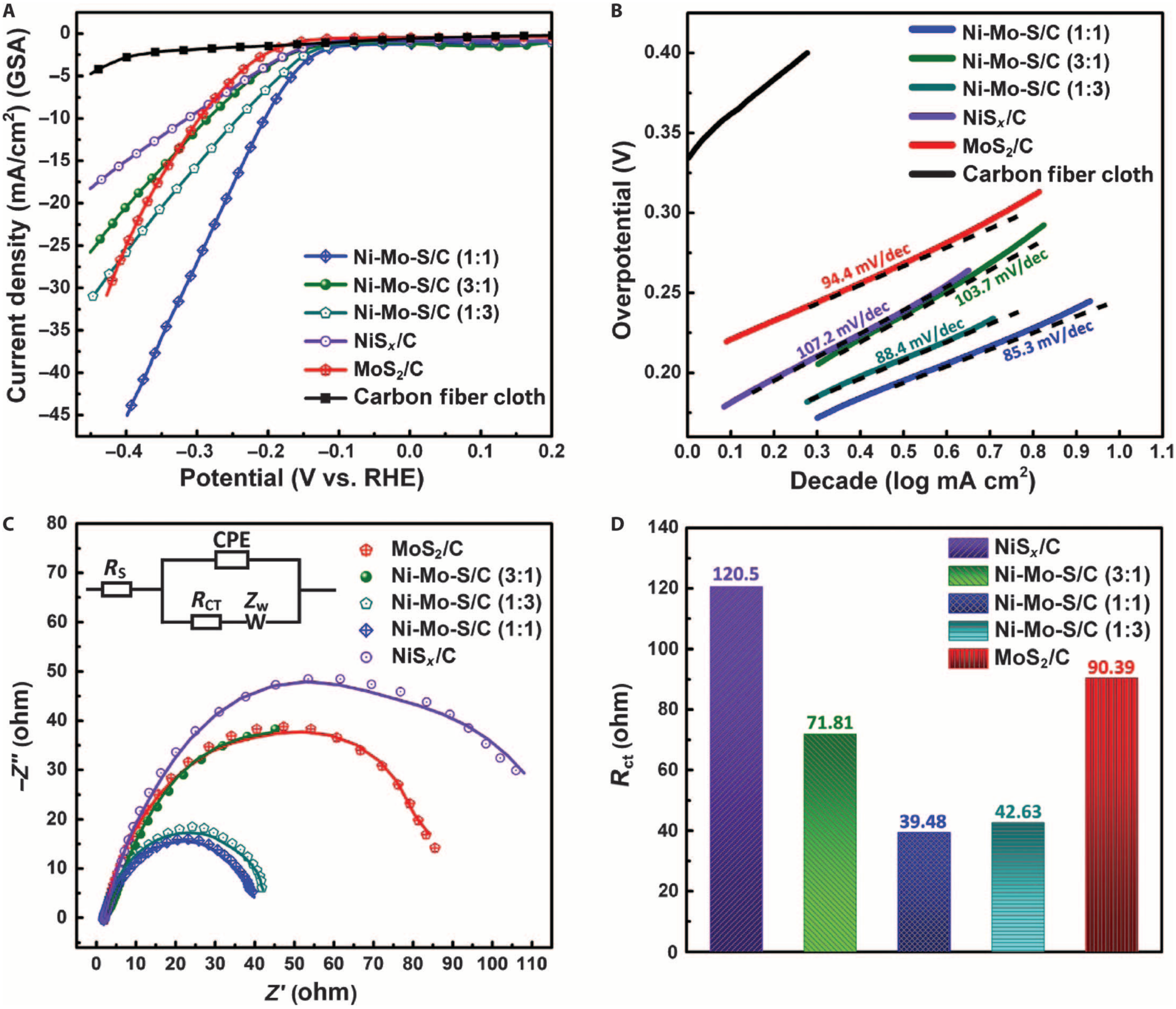

Fig. 8. Electrochemical performances. (**A**) Polarization curves of carbon fiber cloth, NiS$_x$/C, MoS$_2$/C, and different Ni-Mo-S/C in neutral electrolyte. GSA, geometric surface area. (**B**) Corresponding Tafel plots obtained using slow-scan rate polarization curves. (**C**) Electrochemical impedance spectra of different electrodes at −0.3 V versus RHE. Inset: Equivalent circuit used for data analyses. CPE, constant-phase element; Z$_W$, Warburg impedance. (**D**) Plot of charge transport resistance of different samples.

Ni-Mo-S/C (1:1) still shows the best catalytic performance characterized by a low onset overpotential (~−0.14 V) and a reasonably small Tafel slope (~48 mV/dec). The Tafel slope values obtained in acidic electrolyte are closer to those previously reported (*17*, *19*, *41*, *42*), indicating that electrochemical desorption (Heyrovsky reaction) is the rate-determining step for HER catalyzed by Ni-Mo-S/C (1:1) through the Volmer-Heyrovsky mechanism.

Moreover, electrochemical impedance spectroscopy (EIS) analyses were performed to study the electrode kinetics of these samples under the HER mode (*39*, *43*). All measurements were performed at −0.3 V versus RHE from 100 K to 0.1 Hz with alternating current (AC) amplitude of 15 mV in neutral buffer (Fig. 8C). A Randle circuit (inset in Fig. 8C), which is commonly used in analyzing charge transport on single electrodes, was used to fit our experimental results (*44*). All electrodes show small and similar series resistance (R_s), from 1.9 to 2.2 ohms, mainly originated from uncompensated solution resistance, suggesting that our experimental setup was consistent. The slight variation of R_s in different electrodes can be partially attributed to the differences in electrode resistance. The kinetics of electrocatalysis on different electrodes can be reflected from their charge transfer resistance (R_{ct}), and a lower R_{ct} value corresponds to a faster reaction rate (*39*). The R_{ct} values of MoS$_2$/C, NiS$_x$/C, and all Ni-Mo-S/C electrodes are summarized in

Table 1. Calculation of actual catalyst loadings in MoS_2/C, NiS_x/C, and different Ni-Mo-S/C samples.

Sample	Calculated mass loading (mg/cm^2)				SD
	Test 1	Test 2	Test 3	Average	
MoS_2	1.64	1.56	1.63	1.61	0.04
Ni-Mo-S/C (Ni/Mo, 1:3)	0.96	0.84	0.87	0.89	0.06
Ni-Mo-S/C (Ni/Mo, 1:1)	0.52	0.54	0.5	0.52	0.02
Ni-Mo-S/C (Ni/Mo, 3:1)	0.35	0.31	0.3	0.32	0.03
NiS_x	0.44	0.37	0.42	0.41	0.04

Fig. 8D, and show a similar tendency to that previously observed in HER tests (Fig. 8A), with Ni-Mo-S/C (1:1) exhibiting the lowest R_{ct} of 39.48 ohms.

The onset potentials of different samples were measured using the tangent method. As shown in Fig. 9A, the determined onset potentials of Ni-Mo-S/C (1:1) and MoS_2/C are −0.132 and −0.193 V versus RHE, respectively, in neutral electrolyte. Compared to MoS_2/C, the absolute onset potential value of Ni-Mo-S/C (1:1) is 61 mV smaller, arising from its significantly improved HER catalytic activity. However, it is not always fair to judge the catalytic behavior on different electrodes solely on the basis of their differences in onset potential and Tafel slope, especially for the practical gas-evolving reaction. Therefore, we developed a simple strategy that allows us to intuitively compare the onset potentials and gas-evolving profiles of different electrodes at the same time. As shown in fig. S13, a special electrode was designed to visualize the HER processes simultaneously taking place on different samples. Single bundles of MoS_2/C and Ni-Mo-S/C (1:1) with the same length (2 cm) and similar appearance were first extracted from their corresponding carbon fiber cloth electrodes and then firmly attached to the same home-made titanium (Ti) connector. Within the Ti connector, the distance between the ends of two samples was fixed at 3 mm for ease of comparison, whereas the angle between the two bundles was set at 30° for better observation of the gas-evolving events along their entire length. The HER study was then carried out using the parallel linked single-bundle electrodes as the working electrode, in which the synchronized potential bias can be simultaneously applied to MoS_2/C and Ni-Mo-S/C (1:1). In a typical comparative test, the working electrode was linearly swept in a potential window of 0 to −0.8 V versus RHE at a scan rate of 10 mV/s using LSV technique, and the whole process was recorded using a digital camera (movie S2). The first observable gas bubbles were found on Ni-Mo-S/C (1:1) and MoS_2/C at −0.13 and −0.2 V versus RHE, respectively (fig. S14, A and B), matching well with the results obtained from electrochemical tests (Fig. 9A). During the test, H_2 bubbles on Ni-Mo-S/C (1:1) were generated faster and more continuously along the entire bundle. At larger applied biases (−0.8 to −0.4 V versus RHE), it was found that the color of MoS_2/C bundle turned pale white because of the adhesion of numerous freshly evolved gas bubbles (fig. S14C), whereas the appearance of Ni-Mo-S/C bundle (1:1) remained consistent throughout the test with a much more fluent gas-evolving profile. The macroscopic differences between the two electrodes observed by naked eyes originate from their microscopic distinctions. The aggregates formed in MoS_2/C, as discussed above, may evidently decrease the exposed active sites, leading to the attenuated catalytic activity. Meanwhile, these bulky structures will also hinder the effective proton adsorption and H_2 desorption processes because of the presence of trapped bubbles within them. Therefore, the microscopic gas bubbles have to gain their volume before they can be successfully released from these trap sites. Furthermore, these accumulated bubbles on the surface of MoS_2/C will make the electrode less aerophobic and more hydrophobic in appearance, as observed during the test. In brief, a significant decrease in overall efficiency is expected when all these unfavorable factors are combined. In contrast, the significantly improved catalytic performance of Ni-Mo-S/C (1:1) results from the exposure of abundant uniform edge structures along with additional active sites arising from the defect sites in the basal plane, whereas the more fluent gas-evolving profile observed on it may benefit from its sharper and thinner edges, which will ease the gas-releasing (desorption) process (*22*).

To affirm that the catalytic enhancement mainly originates from the more exposed edge sites and defects formed along the basal planes, it is necessary to normalize the electrode HER activities of MoS_2/C and Ni-Mo-S/C (1:1) to their total electrochemically active surface area (EASA). To obtain the total EASA, cyclic voltammetry at different scan rates was performed to calculate the electrochemical double layer capacitance according to the method discussed by Trasatti and Petrii (*45*). More recently, this method was also used by Benck *et al.* to calculate the EASA of MoS_2-based HER catalysts (*46*). In our case, the capacitive current of MoS_2/C and Ni-Mo-S/C (1:1) was measured in 0.5 M sodium phosphate buffer solution at different scan rates (1 to 10, 15, 20, and 25 mV/s) in a potential range from −0.02 to 0.08 V versus saturated calomel electrode (SCE), because there are no obvious electrochemical features corresponding to the faradaic current within this range. The nonfaradaic capacitive current, which is proportional to both the scan rate and EASA, can be calculated from these two sets of CV curves as shown in fig. S15 (A and B). The capacitive current of the two electrodes measured at 0.03 V versus SCE was plotted as a function of scan rate as shown in fig. S15C. We noticed that the dependence of the current on the scan rate in this region is linear for both electrodes, which is consistent with the capacitive charging behavior. From the slope of the linear curve, the unit electrode capacitance was calculated to be 82.78 and 27.74 mF/cm^2 for MoS_2/C and Ni-Mo-S/C (1:1), respectively. In most previously reported studies, the calculated capacitance of single-layer/flat MoS_2 is ~60 μF/cm^2 (*46*). With this number, the total EASAs of MoS_2/C and Ni-Mo-S/C (1:1) are 1379.67 and 462.33 cm^2, respectively, on the electrodes with a geometric area of ~1 cm^2. This result suggests that the total EASA of MoS_2/C is three times that of Ni-Mo-S/C (1:1). Figure S15D shows the polarization curves of MoS_2/C and Ni-Mo-S/C (1:1) normalized by their corre-

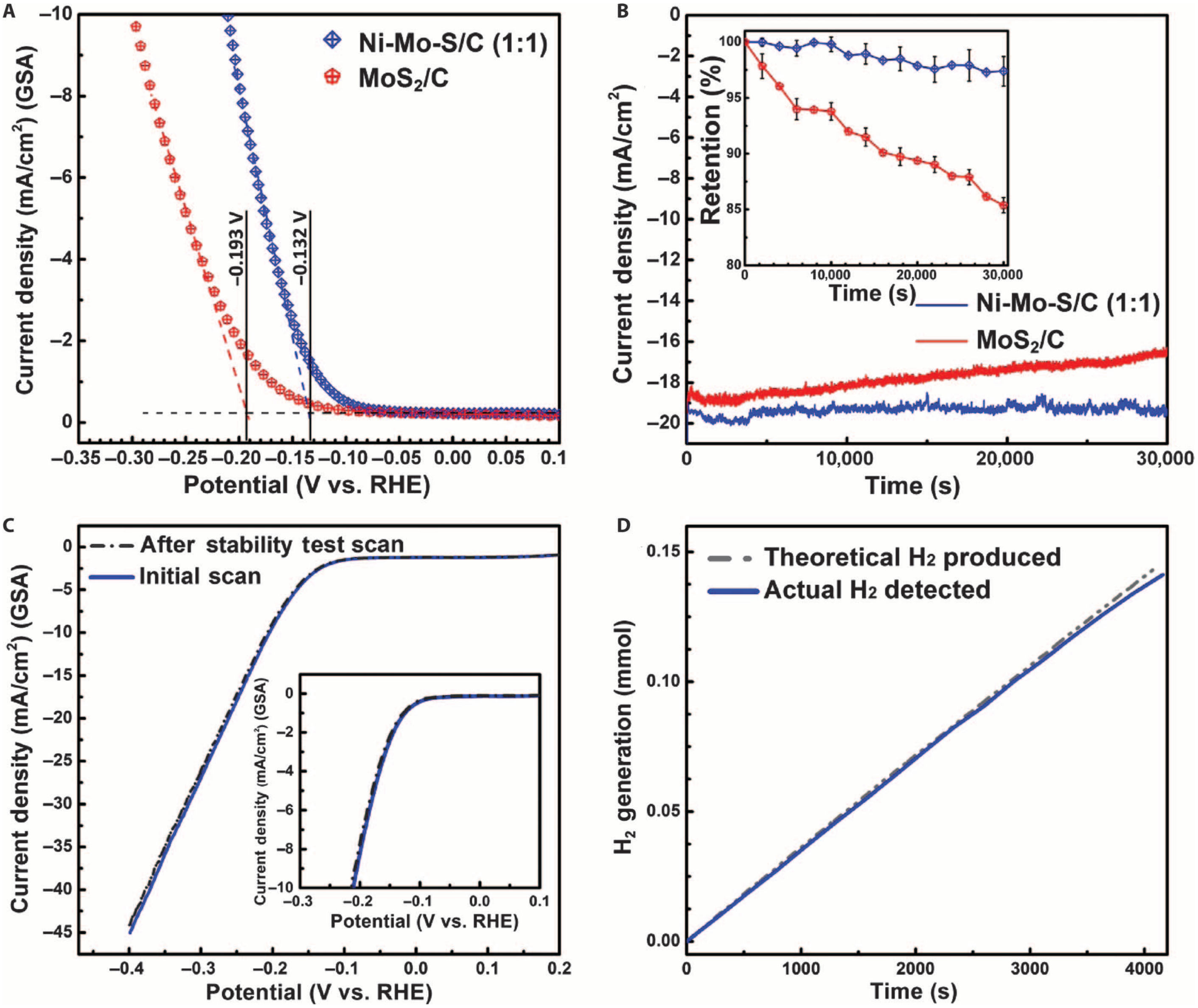

Fig. 9. Electrochemical hydrogen evolution tests. (**A**) Onset comparison between MoS$_2$/C and Ni-Mo-S/C (1:1). (**B**) Stability tests of Ni-Mo-S/C (1:1) and MoS$_2$/C in neutral electrolyte. (**C**) LSV curves of Ni-Mo-S/C (1:1) before and after stability tests. (**D**) Comparison of the detected amount of evolved H$_2$ and the theoretical value in Faraday efficiency measurement.

sponding total EASA, confirming that the performance of Ni-Mo-S/C (1:1) is significantly better than its counterpart. These results suggest that there would be many more active sites on Ni-Mo-S/C (1:1) as compared to MoS$_2$/C on the electrodes with the same EASA. Besides the EASA measurements, the edge-rich feature of Ni-Mo-S/C (1:1) was also confirmed using the irreversible electrochemical oxidation method proposed by Bonde *et al.* (*47*). (Refer to fig. S16 and note S2 in the Supplementary Materials.)

Stability is another critical factor for designing gas-evolving electrodes that are eligible for long-term operation. In our work, the durability of Ni-Mo-S/C (1:1) and MoS$_2$/C electrodes (1 × 1 cm) was assessed using controlled potential electrolysis in neutral electrolyte. The two electrodes were operated at their corresponding η_{20} (overpotential at current density of 20 mA/cm^2) for 30,000 s. Continuous gas bubbling was observed on both Ni-Mo-S/C (1:1) and MoS$_2$/C throughout the test. As shown in Fig. 9B, Ni-Mo-S/C (1:1) can retain about 97.5% of its initial current density after the test, which is apparently better than the 85% current density retention of MoS$_2$/C. For comparison, we also performed the stability of commercial Pt plate electrode (1 × 1 cm) in neutral electrolyte. It was found that only 15% of the initial current density was retained after 1-hour controlled potential electrolysis (fig. S17). The rapid deactivation of Pt in neutral buffer electrolyte might be due to the poisoning effect of phosphoric acid anions (see fig. S18 and note S3). The excellent stability of Ni-Mo-S/C (1:1) was further affirmed using LSV technique after controlled potential electrolysis. As shown in Fig. 9C, the polarization curve obtained after a stability test was almost identical with the initial scan, without obvious shift in onset potential and curve shapes. In addition, as shown in fig. S19, no obvious changes in the oxidation states of Mo, S, and Ni were detected in the XPS measurements after the stability test, affirming the excellent stability of Ni-Mo-S/C (1:1).

The Faraday efficiency of Ni-Mo-S/C (1:1) was measured using a multipurpose compact glass photo-/electrocatalysis reactor, integrated with a single-chamber bulk electrolysis cell. The schematic and photographs of the experimental setup are shown in figs. S20 and S21, respectively. Controlled potential electrolysis was performed on Ni-Mo-S/C (1:1) in neutral electrolyte, with a moderate applied bias of –0.2 V versus RHE for 4000 s. The detailed Faraday efficiency calculation steps are described in the Supplementary Materials (note S4). Figure 9D shows that the actual detected H_2 amount was correlated with the theoretical value calculated on the basis of the charge transferred, resulting in a high Faraday efficiency of 98.2%. From the gas chromatography (GC) spectra, H_2 and O_2 (evolved on graphite foil) were the only two gaseous products detected throughout the test, which affirms the capability of Ni-Mo-S/C (1:1) as an HER electrode in producing high-purity H_2 gas.

To further demonstrate the potential of Ni-Mo-S/C in practical applications, a simple prototype of laboratory-scale hydrogen generator was designed. Figures S22 and S23 show the schematic and actual assembly of the laboratory-scale Ni-Mo-S/C hydrogen generator, respectively. To prepare this reactor, a piece of Ni-Mo-S/C (1:1) (2 × 4 cm) was first rolled up into a column shape and then firmly fixed on a homemade Ti holder, which also worked as the lead and electrode connector (fig. S23B). A 5-ml sterile round-bottom tube was used as the electrode housing and the primary gas collector (fig. S23C). The Ti holder together with the clamped Ni-Mo-S/C was loaded into the tube and fixed using Scotch tape. To integrate the reactor with the gas-evacuation system or secondary gas collector, a round hole with a diameter of 1 mm was drilled on its top. Here, a 5-ml syringe, functioning as a simplified gas-evacuation system, was tightly sealed onto the reactor (fig. S23D). For the practical operation, the H_2 generator should be vertically inserted into the electrolyte. The air remaining in the tube was then evacuated using the syringe, whereas the electrolyte was sucked upward to fill the entire tube. When the system is operated at a moderate bias of –0.5 V versus RHE, the 5-ml tube can be filled with H_2 in ~150 s (movie S3).

On the basis of experimental findings, we propose a hypothetical growth mechanism to explicate the development of a high-performance Ni-Mo-S HER electrocatalyst. Without the incorporation of Ni^{2+}, the growth of layered MoS_2 crystals proceeds in a fast and uncontrollable fashion. The rapidly grown MoS_2 sheets tend to aggregate in solution, thus leading to the formation of bulky coalescences. We noticed that the morphological evolution of Ni-Mo-S/C strongly depended on the Ni-to-Mo precursor ratio. It is believed that the introduced Ni^{2+} could bond to the free sulfur during the growth or nucleation of MoS_2 nanocrystals, subsequently leading to the formation of substitutional and Schottky defects that instantly interrupt the regular atomic arrangement in MoS_2. The formation of Ni-S bonds was confirmed by x-ray absorption measurement (fig. S24), in which the Ni-S path (~2.23 Å) has a smaller atomic radius than the Mo-S path (~2.39 Å). Note that this difference can be attributed to the ionic radial discrepancy between Mo^{4+} (70 pm) and Ni^{2+} (83 pm), which is consistent with the observation from XPS (Fig. 7). As a classic hydrodesulfurization catalyst model, the Co-Mo-S has been thoroughly studied over the past few decades (*13*, *48*–*50*). On the basis of the density function theory, Byskov *et al.* found that the substitutional Co atoms in Co-Mo-S resulted in significantly lower sulfur binding energy as well as shorter bond length near the vacancies (*51*). In our case, Ni atoms will play similar roles in tuning the Ni-Mo-S framework, that is, the change in bond length and binding energy near the incorporated Ni atoms may lead to an extensive distortion across the basal plane, thus hindering the rapid growth of a continuous MoS_2 film, while creating extra edges with more exposed active sites.

Figure S25 shows the schematic illustration of a MoS_2 nanocrystal surrounded by Ni^{2+} executing Brownian motion, where Ni could be incorporated into the existing MoS_2 framework upon its successful collision with the free sulfur ends. The distribution of Ni^{2+} around the MoS_2 nanocrystals is critical in determining the eventually evolved morphology of Ni-Mo-S structure on carbon fibers, because the frequency of successful bond formation largely depends on their concentrations, according to the collision theory in chemical kinetics (*52*). When MoS_2 nanocrystals are surrounded by excessive Ni^{2+} ions, vigorous collisions may take place, thus accelerating the formation of substitutional and vacancy defects, which, in turn, constrain the continuous growth of the layered structure of Ni-Mo-S. On the contrary, the inadequate Ni^{2+} will only introduce random allocated defect sites with lower density, which cannot significantly alter the growth of the layered structures observed in MoS_2. These assumptions explain the morphological evolution that we observed in different Ni-Mo-S/C samples well (Figs. 2 and 3). Optimum Ni-to-Mo precursor ratio will lead to the formation of moderate defect sites along the basal plane, which simultaneously introduce additional active sites and constrain the growth rate of Ni-Mo-S layers. On the basis of these assumptions, we constructed the models of MoS_2 and Ni-Mo-S and performed molecular mechanical simulation (molecular mechanics + force field) using HyperChem (*10*). Figure S26 (A and B) shows the molecular models after geometric optimization for MoS_2 and Ni-Mo-S, respectively. Compared to the pristine MoS_2, the random defects formed in Ni-Mo-S can cause a significant geometric distortion on the basal plane because of the change in bond length and the presence of vacancies. The increase in molecular complexity along with the distortions across the entire basal plane may further weaken the interaction between the adjacent Ni-Mo-S layers, thus leading to an enlargement of the interlayer spacing (fig. S26D), which is consistent with the observation in Fig. 4D. On the basis of these findings, we know that optimizing the Ni-to-Mo precursor ratio is important in tailoring the nanostructure of Ni-Mo-S at atomic scale. Apart from the structural effects, the incorporated Ni atoms may also function as promoters that further enhance the intrinsic catalytic activities, especially in neutral electrolyte, similar to that proposed by Merki *et al.* (*39*). Besides, Lin *et al.* reported the atomic mechanism of the semiconducting (2H)–to–metallic (1T) phase transition in single-layered MoS_2 (*10*). In our case, the bond-length shortening introduced by the Ni atom may also initiate the gliding of a sulfur plane near the defect sites, further resulting in the localized phase transition that partially converts 2H MoS_2 to metastable 1T MoS_2. As previously discussed by Lukowski *et al.*, the metallic 1T MoS_2 may exhibit enhanced electrocatalytic activity along with the improved stability (*53*). In addition, the incorporation of Ni atoms may alter the binding energy of pristine MoS_2, further improving the reaction kinetics.

Table 2. Preparation of MoS_2, NiS_x, and Ni-Mo-S on carbon fiber cloth.

Precursor sample	$Na_2MoO_4·2H_2O$ (25 mM) (ml)	$NiSO_4·6H_2O$ (25 mM) (ml)	L-Cys (132 mM) (ml)
MoS_2	20	0	20
Ni-Mo-S (Ni/Mo, 1:3)	15	5	20
Ni-Mo-S (Ni/Mo, 1:1)	10	10	20
Ni-Mo-S (Ni/Mo, 3:1)	5	15	20
NiS_x	0	20	20

DISCUSSION

In conclusion, we have developed a facile synthetic strategy to directly grow nanostructured Ni-Mo-S on carbon fiber cloth as a high-efficiency functional electrode for hydrogen generation in neutral electrolyte. The incorporated Ni atoms play vital roles in constructing Ni-Mo-S nanostructures through forming substantial desirable defect sites as well as regulating the growth rate of layered MoS_2. The optimized Ni-Mo-S/C exhibits excellent HER catalytic performance, characterized by its low onset potential of −0.132 V versus RHE and a small Tafel slope of 85.3 mV/dec in the neutral electrolyte. The reduced stacking and aggregations in Ni-Mo-S/C effectively prevent the accumulation of instantly evolved H_2 bubbles during electrolysis, hence improving the performance and stability of Ni-Mo-S/C in long-term hydrogen production. The remarkable HER performance in acidic and neutral media of Ni-Mo-S/C is comparable with other state-of-the-art HER electrocatalysts (see tables S2 and S3). To further demonstrate its potential application in practical appliances, a laboratory-scale hydrogen generator with a rolled Ni-Mo-S/C electrode was designed to carry out the potential controlled electrolysis. Owing to the ultimate flexibility and excellent mechanical strength offered by the carbon fiber cloth, the functional Ni-Mo-S/C electrode developed in this work should be easily integrated into existing H_2 generators with appropriate modification to meet their specified standards and requirements. To carry out more practical application, we also performed HER tests using Ni-Mo-S/C (1:1) in real seawater (see note S5 and figs. S27 and S28 in the Supplementary Materials). We believe that better electrode performance could be achieved through engineering the carbon fiber cloth, for example by widening the interstrand spacing and reducing the packing density of the carbon fiber.

MATERIALS AND METHODS

Materials

Woven carbon fiber cloth with evenly sized pores was purchased from GasHub Technology. Sodium molybdate dihydrate ($Na_2MoO_4 \cdot 2H_2O$), nickel sulfate hexahydrate ($NiSO_4 \cdot 6H_2O$), L-Cys ($HSCH_2CHNH_2COOH$), sulfuric acid (H_2SO_4, ≥98%), sodium phosphate monobasic (NaH_2PO_4), and sodium phosphate dibasic (Na_2HPO_4) were purchased from Sigma-Aldrich. Hydrogen peroxide (H_2O_2) was purchased from Alfa Aesar, and acetone [$(CH_3)_2CO$] was purchased from Acros Organics. All chemical reagents were directly used without further purification. Milli-Q water (resistivity over 18 megohm·cm) from a Millipore Q water purification system was used in all experiments.

Syntheses of MoS_2 and Ni-Mo-S on carbon fiber cloth

Carbon fiber cloth substrates were consecutively washed with acetone, H_2SO_4 (1 M), and deionized water under sonication for 2 hours in each solution to thoroughly remove organic residues and other impurities. The substrates were then soaked in "piranha" solution, that is, a mixture of concentrated sulfuric acid and 30% hydrogen peroxide with a volume ratio of 3:1, overnight to further improve their hydrophilicity. The clean substrates were kept in Milli-Q water to avoid regaining hydrophobicity.

The MoS_2, NiS_x, and Ni-Mo-S were grown on the cleaned carbon fiber cloth using a biomolecule-assisted hydrothermal synthetic route. Briefly, sodium molybdate dihydrate ($Na_2MoO_4 \cdot 2H_2O$) and nickel sulfate hexahydrate ($NiSO_4 \cdot 6H_2O$) were used as Mo and Ni sources, respectively, whereas L-Cys ($HSCH_2CHNH_2COOH$) was used as an S source and reducing agent. To study the effect of the Ni-to-Mo precursor ratio on the morphology and performance of the as-prepared functional electrodes, $Na_2MoO_4 \cdot 2H_2O$ (6.05 mg/ml, 25 mM), $NiSO_4 \cdot 6H_2O$ (6.57 mg/ml, 25 mM), and L-Cys (16 mg/ml, 132 mM) aqueous solutions were prepared and mixed according to Table 2, whereas the sum of molar amounts of Ni and Mo was kept constant in the precursor solutions for all samples.

The precursor solutions have to be rapidly mixed and subjected to vigorous stirring to prevent the formation of precipitates. Then, the solution was transferred to a 50-ml Teflon-lined stainless autoclave. Thereafter, a piece of precleaned carbon fiber cloth was vertically aligned in the growth solution. The autoclave was heated at 200°C for 24 hours. After naturally cooling down to room temperature, the sample was thoroughly washed with Milli-Q water and dried using compressed airflow at room temperature. The weight of carbon fiber cloth electrodes was precisely recorded before and after reaction using an Ohaus analytical balance to calculate the actual catalyst-loading amount. The calculation of actual loadings for MoS_2/C, NiS_x/C, and different Ni-Mo-S/C samples can be found in Table 1.

Sample characterization

The morphology and elemental composition of samples were examined using field emission SEM (JEOL JSM-6700F), TEM (JEOL JEM-3010), and EDS (JEOL JED-2300 Analysis Station). BET measurements were performed using the Autosorb-1 system (Quantachrome Instruments). XRD measurements were conducted on the Bruker AXS D8 Advance and D2 Phaser to study the crystal structures and phase compositions. XPS measurements were carried out on an ESCALAB 250 photoelectron spectrometer (Thermo Fisher Scientific) at 2.4×10^{-10} mbar using a monochromatic Al Kα x-ray beam (1486.60 eV). All binding energies were referenced to the C 1*s* peak (284.60 eV) arising from the adventitious hydrocarbons. Raman spectra of the samples were measured using a research laser Raman microscope (Renishaw RM1000), with a 514.5-nm excitation laser. The Raman band of Si at 520 cm^{-1} was used as the reference to calibrate the spectrometer. A series of extended x-ray absorption fine structure (EXAFS) measurements were made using synchrotron radiation. Measurements were made at the Ni K edge (8333 eV) and the Mo K edge (20,000 eV) with the sample held at room temperature. The 01C beamline in the National Synchrotron Radiation Research Center in Taiwan was designed for such experiments. The backscattering amplitude and phase shift functions for specific atom pairs were calculated ab initio using the FEFF8 code. X-ray absorption data were analyzed following standard procedures, including pre- and post-edge background subtraction, normalization with respect to edge height, Fourier transformation, and nonlinear least-squares curve fitting. The normalized k^3-weighted EXAFS spectra, $k^3x(k)$, were Fourier-transformed in the k range from 3.1 to 12.7 Å^{-1} to reveal the contribution of each bond pair on the Fourier transform peak. The experimental Fourier-filtered spectra were obtained by performing an inverse Fourier transformation with a Hanning window function with r between 1.1 and 2.4 Å. The $S_0{}^2$ (amplitude reduction factor) values of Mo and Ni atoms were fixed at 0.9 and 0.91 to determine the structural parameters of each bond pair.

Electrochemical measurements

Electrochemical measurements were carried out on an electrochemical workstation (CHI 760E) with a three-electrode setup, consisting of an as-prepared electrode as the working electrode, a graphite foil (2 × 3 cm) as the counter electrode, and an SCE (in saturated KCl) as the reference electrode. To assess the catalytic activity in neutral medium, electrochemical tests were primarily carried out in 0.5 M sodium phosphate buffer solution prepared by mixing 0.5 M NaH_2PO_4 and 0.5 M Na_2HPO_4 aqueous solutions with an appropriate ratio. The HER performance was also studied in 0.5 M H_2SO_4 electrolyte. The electrolytes were deaerated by purging nitrogen for 30 min before the electrochemical measurement. The pH of different electrolytes was carefully measured using a calibrated pH meter (Mettler Toledo SevenCompact), resulting in 0.18 and 6.94 for 0.5 M H_2SO_4 and 0.5 M sodium phosphate buffer solution, respectively.

The reference electrode calibration was performed using a standard Pt plate electrode as the working electrode. Cyclic voltammetry scans were performed at a scan rate of 1 mV/s, and the average of the two potentials at which the current crossed zero was taken as the experimentally determined 0 V versus RHE (or $V_{\mathrm{HOR/HER}}$). On the basis of this value, the electrode potential of the SCE that was used in this work was obtained by using the following equation:

$$V^0_{\mathrm{SCE}}(\mathrm{V}) = V_{\mathrm{HOR/HER}} - 0.059\ \mathrm{V} \times \mathrm{pH}.$$

The theoretical electrode potential of SCE (in saturated KCl) was reported to be 0.241 to 0.244 V versus RHE. But the values that we determined experimentally, that is, 0.238 V versus RHE in 0.5 M H_2SO_4 and 0.234 V versus RHE in 0.5 M sodium phosphate buffer solution, slightly differ from the theoretical values.

The catalytic behaviors of different materials were studied and compared using LSV at a scan rate of 5 mV/s, whereas the stability was studied using amperometric technique. The measured voltage values were converted to RHE scale by applying the following calculation:

$$V_{\mathrm{RHE}} = V_{\mathrm{measured}} + V^0_{\mathrm{SCE}} + 0.059 \times \mathrm{pH},$$

where V_{RHE} is the converted potential value versus RHE, V_{measured} is the voltage reading from potentiostat, and $V^0{}_{\mathrm{SCE}}$ is the experimentally determined electrode potential of SCE.

To study the electrode kinetics, EIS was performed at −0.3 V versus RHE in a range from 100 K to 0.1 Hz with an AC amplitude of 15 mV, using an electrochemical workstation (Zive SP2, WonATech). The data were analyzed and fitted in equivalent circuits using ZView software, and Nyquist plots were used to study the charge transport properties.

Here, AC impedance technique was used to obtain the uncompensated resistance (R_u) of the working electrodes before the LSV measurements. All polarization curves were iR-corrected with a compensation level of 90%.

Faraday efficiency measurement

Faraday efficiency measurement was performed inside a multipurpose compact glass photo-/electrocatalysis reactor, integrated with a single-chamber electrolysis cell. The sample line of the reactor was linked to an online GC (Agilent 490), which is equipped with a molecular sieve column and a thermal conductivity detector, allowing the real-time detection of gas products. Inside the electrolysis cell, the Ni-Mo-S/C, graphite foil, and SCE were used as working, counter, and reference electrodes, respectively, whereas deaerated 0.5 M sodium phosphate buffer was used as the electrolyte. Before the measurement, the system was thoroughly evacuated using a high-efficiency vacuum pump and then charged with ultrapure argon (Ar, 99.9995%) gas to 1 atm. Constant potential was applied to the working electrode using an electrochemical workstation (CHI 760E). The compositions and concentrations of the gas products were analyzed with GC through automatic sampling every 4 min.

SUPPLEMENTARY MATERIALS

Supplementary material for this article is available at http://advances.sciencemag.org/cgi/content/full/1/7/e1500259/DC1

Fig. S1. SEM image of carbon fiber cloth.
Fig. S2. SEM image of MoS_2/C synthesized with reduced precursor concentration.
Fig. S3. SEM images of MoS_2/C synthesized after different durations of hydrothermal treatment.
Fig. S4. SEM images of NiS_x/C.
Fig. S5. SEM images of aggregates.
Fig. S6. EDS spectra of different samples.
Fig. S7. Point EDS spectra of Ni-Mo-S/C (3:1).
Fig. S8. HRTEM images of Ni-Mo-S/C (1:1).
Fig. S9. Elemental mapping of Ni-Mo-S/C (1:1).
Fig. S10. BET measurements of Ni-Mo-S/C (1:1).
Fig. S11. Normalized current density.
Fig. S12. HER tests in 0.5 M H_2SO_4.
Fig. S13. Electrode for intuitive comparison test.
Fig. S14. Intuitive comparison test for HER.
Fig. S15. EASA measurements for MoS_2/C and Ni-Mo-S/C (1:1).
Fig. S16. Irreversible electrochemical oxidation cyclic voltammetry curves.
Fig. S17. HER stability of Pt in neutral electrolyte.
Fig. S18. XPS spectra of fresh and deactivated Pt plate electrodes.
Fig. S19. High-resolution XPS spectra of Ni-Mo-S/C (1:1) after stability test.
Fig. S20. Experimental setup for Faraday efficiency test.
Fig. S21. Actual experimental setup for Faraday efficiency measurement.
Fig. S22. Laboratory-scale Ni-Mo-S/C hydrogen generator.
Fig. S23. Assembly of laboratory-scale Ni-Mo-S/C hydrogen generator.
Fig. S24. EXAFS spectra of Ni-Mo-S/C (1:1).
Fig. S25. Formation mechanism of Ni-Mo-S nanostructure.
Fig. S26. Molecular models.
Fig. S27. Collection of seawater.
Fig. S28. HER of Ni-Mo-S/C (1:1) in seawater.
Note S1. Brief explanation on the aggregation mechanism of MoS_2 nanostructures.
Note S2. Irreversible electrochemical oxidation of MoS_2/C and Ni-Mo-S/C (1:1).
Note S3. XPS study of the rapid deactivation of Pt in neutral buffer electrolyte.
Note S4. Faraday efficiency calculation.
Note S5. Hydrogen evolution on Ni-Mo-S/C (1:1) in real seawater.
Table S1. Exchange current densities of MoS_2/C, NiS_x/C, and different Ni-Mo-S/C samples in neutral electrolyte.
Table S2. Comparison of electrocatalysts for HER in neutral or near-neutral electrolytes.
Table S3. Comparison of various MoS_x-based electrocatalysts for HER.
Movie S1. Hydrogen evolution on Ni-Mo-S/C (1:1) electrode in neutral electrolyte.
Movie S2. Intuitive comparison test for HER.
Movie S3. Laboratory-scale Ni-Mo-S/C (1:1) hydrogen generator.
References (*54–68*)

REFERENCES AND NOTES

1. M. G. Walter, E. L. Warren, J. R. McKone, S. W. Boettcher, Q. Mi, E. A. Santori, N. S. Lewis, Solar water splitting cells. *Chem. Rev.* **110**, 6446–6473 (2010).
2. A. Lasia, Hydrogen evolution reaction, in *Handbook of Fuel Cells: Fundamentals, Technology and Applications* (Wiley, New York, NY, 2010), vol. 2, pp. 416–440.
3. B. Hinnemann, P. G. Moses, J. Bonde, K. P. Jørgensen, J. H. Nielsen, S. Horch, I. Chorkendorff, J. K. Nørskov, Biomimetic hydrogen evolution: MoS_2 nanoparticles as catalyst for hydrogen evolution. *J. Am. Chem. Soc.* **127**, 5308–5309 (2005).
4. B. E. Conway, B. V. Tilak, Interfacial processes involving electrocatalytic evolution and oxidation of H_2, and the role of chemisorbed H. *Electrochim. Acta* **47**, 3571–3594 (2002).
5. X. Huang, Z. Zeng, H. Zhang, Metal dichalcogenide nanosheets: Preparation, properties and applications. *Chem. Soc. Rev.* **42**, 1934–1946 (2013).
6. X. Huang, C. Tan, Z. Yin, H. Zhang, 25th Anniversary article: Hybrid nanostructures based on two-dimensional nanomaterials. *Adv. Mater.* **26**, 2185–2204 (2014).
7. H. Li, J. Wu, Z. Yin, H. Zhang, Preparation and applications of mechanically exfoliated single-layer and multilayer MoS_2 and WSe_2 nanosheets. *Acc. Chem. Res.* **47**, 1067–1075 (2014).
8. K. Chang, W. Chen, L-Cysteine-assisted synthesis of layered MoS_2/graphene composites with excellent electrochemical performances for lithium ion batteries. *ACS Nano* **5**, 4720–4728 (2011).
9. X. Cao, Y. Shi, W. Shi, X. Rui, Q. Yan, J. Kong, H. Zhang, Preparation of MoS_2-coated three-dimensional graphene networks for high-performance anode material in lithium-ion batteries. *Small* **9**, 3433–3438 (2013).
10. Y.-C. Lin, D. O. Dumcenco, Y.-S. Huang, K. Suenaga, Atomic mechanism of the semiconducting-to-metallic phase transition in single-layered MoS_2. *Nat. Nanotechnol.* **9**, 391–396 (2014).
11. B. Radisavljevic, A. Radenovic, J. Brivio, V. Giacometti, A. Kis, Single-layer MoS_2 transistors. *Nat. Nanotechnol.* **6**, 147–150 (2011).
12. Z. Yin, H. Li, H. Li, L. Jiang, Y. Shi, Y. Sun, G. Lu, Q. Zhang, X. Chen, H. Zhang, Single-layer MoS_2 phototransistors. *ACS Nano* **6**, 74–80 (2012).
13. L. S. Byskov, J. K. Nørskov, B. S. Clausen, H. Topsøe, DFT calculations of unpromoted and promoted MoS_2-based hydrodesulfurization catalysts. *J. Catal.* **187**, 109–122 (1999).
14. X. Huang, Z. Zeng, S. Bao, M. Wang, X. Qi, Z. Fan, H. Zhang, Solution-phase epitaxial growth of noble metal nanostructures on dispersible single-layer molybdenum disulfide nanosheets. *Nat. Commun.* **4**, 1444 (2013).
15. H. Tributsch, J. Bennett, Electrochemistry and photochemistry of MoS_2 layer crystals. I. *J. Electroanal. Chem. Interfacial Electrochem.* **81**, 97–111 (1977).
16. A. Sobczynski, Molybdenum disulfide as a hydrogen evolution catalyst for water photodecomposition on semiconductors. *J. Catal.* **131**, 156–166 (1991).
17. A. B. Laursen, S. Kegnæs, S. Dahl, I. Chorkendorff, Molybdenum sulfides–efficient and viable materials for electro- and photoelectrocatalytic hydrogen evolution. *Energy Environ. Sci.* **5**, 5577–5591 (2012).
18. T. F. Jaramillo, K. P. Jørgensen, J. Bonde, J. H. Nielsen, S. Horch, I. Chorkendorff, Identification of active edge sites for electrochemical H_2 evolution from MoS_2 nanocatalysts. *Science* **317**, 100–102 (2007).
19. Y. Li, H. Wang, L. Xie, Y. Liang, G. Hong, H. Dai, MoS_2 nanoparticles grown on graphene: An advanced catalyst for the hydrogen evolution reaction. *J. Am. Chem. Soc.* **133**, 7296–7299 (2011).
20. J. Kibsgaard, Z. Chen, B. N. Reinecke, T. F. Jaramillo, Engineering the surface structure of MoS_2 to preferentially expose active edge sites for electrocatalysis. *Nat. Mater.* **11**, 963–969 (2012).
21. H. Wang, Z. Lu, S. Xu, D. Kong, J. J. Cha, G. Zheng, P.-C. Hsu, K. Yan, D. Bradshaw, F. B. Prinz, Y. Cui, Electrochemical tuning of vertically aligned MoS_2 nanofilms and its application in improving hydrogen evolution reaction. *Proc. Natl. Acad. Sci. U.S.A.* **110**, 19701–19706 (2013).
22. Z. Lu, W. Zhu, X. Yu, H. Zhang, Y. Li, X. Sun, X. Wang, H. Wang, J. Wang, J. Luo, X. Lei, L. Jiang, Ultrahigh hydrogen evolution performance of under-water "superaerophobic" MoS_2 nanostructured electrodes. *Adv. Mater.* **26**, 2683–2687 (2014).
23. J. Xie, H. Zhang, S. Li, R. Wang, X. Sun, M. Zhou, J. Zhou, X. W. Lou, Y. Xie, Defect-rich MoS_2 ultrathin nanosheets with additional active edge sites for enhanced electrocatalytic hydrogen evolution. *Adv. Mater.* **25**, 5807–5813 (2013).
24. J. Xie, J. Zhang, S. Li, F. Grote, X. Zhang, H. Zhang, R. Wang, Y. Lei, B. Pan, Y. Xie, Controllable disorder engineering in oxygen-incorporated MoS_2 ultrathin nanosheets for efficient hydrogen evolution. *J. Am. Chem. Soc.* **135**, 17881–17888 (2013).
25. Y. Zheng, Y. Jiao, M. Jaroniec, S. Z. Qiao, Advancing the electrochemistry of the hydrogen-evolution reaction through combining experiment and theory. *Angew. Chem. Int. Ed.* **54**, 52–65 (2015).
26. J. Duan, S. Chen, M. Jaroniec, S. Z. Qiao, Porous C_3N_4 nanolayers@N-graphene films as catalyst electrodes for highly efficient hydrogen evolution. *ACS Nano* **9**, 931–940 (2015).
27. Y. Zheng, Y. Jiao, Y. Zhu, L. H. Li, Y. Han, Y. Chen, A. Du, M. Jaroniec, S. Z. Qiao, Hydrogen evolution by a metal-free electrocatalyst. *Nat. Commun.* **5**, 3783 (2014).
28. S. Chen, J. Duan, M. Jaroniec, S.-Z. Qiao, Nitrogen and oxygen dual-doped carbon hydrogel film as a substrate-free electrode for highly efficient oxygen evolution reaction. *Adv. Mater.* **26**, 2925–2930 (2014).
29. X.-L. Li, Y.-D. Li, MoS_2 nanostructures: Synthesis and electrochemical Mg^{2+} intercalation. *J. Phys. Chem. B* **108**, 13893–13900 (2004).
30. K. S. W. Sing, D. H. Everett, R. A. W. Haul, L. Moscou, R. A. Pierotti, J. Rouquérol, T. Siemieniewska, Reporting physisorption data for gas/solid systems with special reference to the determination of surface area and porosity. *Pure Appl. Chem.* **57**, 603–619 (1985).
31. B. D. Cullity, S. R. Stock, Chapter 3: Diffraction I: The directions of diffracted beams, in *Elements of X-ray Diffraction* (Pearson, Upper Saddle River, NJ, 2001), pp. 78–103.
32. L. Cheng, W. Huang, Q. Gong, C. Liu, Z. Liu, Y. Li, H. Dai, Ultrathin WS_2 nanoflakes as a high-performance electrocatalyst for the hydrogen evolution reaction. *Angew. Chem. Int. Ed.* **53**, 7860–7863 (2014).
33. C. Lee, H. Yan, L. E. Brus, T. F. Heinz, J. Hone, S. Ryu, Anomalous lattice vibrations of single- and few-layer MoS_2. *ACS Nano* **4**, 2695–2700 (2010).
34. B. C. Windom, W. Sawyer, D. W. Hahn, A Raman spectroscopic study of MoS_2 and MoO_3: Applications to tribological systems. *Tribol. Lett.* **42**, 301–310 (2011).
35. D. Kong, H. Wang, J. J. Cha, M. Pasta, K. J. Koski, J. Yao, Y. Cui, Synthesis of MoS_2 and $MoSe_2$ films with vertically aligned layers. *Nano Lett.* **13**, 1341–1347 (2013).
36. S. Houssenbay, S. Kasztelan, H. Toulhoat, J. Bonnelle, J. Grimblot, Nature of the different nickel species in sulfided bulk and alumina-supported nickel-molybdenum hydrotreating catalysts. *J. Phys. Chem.* **93**, 7176–7180 (1989).
37. Y. Sun, C. Liu, D. C. Grauer, J. Yano, J. R. Long, P. Yang, C. J. Chang, Electrodeposited cobalt-sulfide catalyst for electrochemical and photoelectrochemical hydrogen generation from water. *J. Am. Chem. Soc.* **135**, 17699–17702 (2013).
38. Z. Chen, D. Cummins, B. N. Reinecke, E. Clark, M. K. Sunkara, T. F. Jaramillo, Core-shell MoO_3-MoS_2 nanowires for hydrogen evolution: A functional design for electrocatalytic materials. *Nano Lett.* **11**, 4168–4175 (2011).
39. D. Merki, H. Vrubel, L. Rovelli, S. Fierro, X. Hu, Fe, Co, and Ni ions promote the catalytic activity of amorphous molybdenum sulfide films for hydrogen evolution. *Chem. Sci.* **3**, 2515–2525 (2012).
40. P. D. Tran, M. Nguyen, S. S. Pramana, A. Bhattacharjee, S. Y. Chiam, J. Fize, M. J. Field, V. Artero, L. H. Wong, J. Loo, J. Barber, Copper molybdenum sulfide: A new efficient electrocatalyst for hydrogen production from water. *Energy Environ. Sci.* **5**, 8912–8916 (2012).
41. D. J. Li, U. N. Maiti, J. Lim, D. S. Choi, W. J. Lee, Y. Oh, G. Y. Lee, S. O. Kim, Molybdenum sulfide/N-doped CNT forest hybrid catalysts for high-performance hydrogen evolution reaction. *Nano Lett.* **14**, 1228–1233 (2014).
42. H. Vrubel, D. Merki, X. Hu, Hydrogen evolution catalyzed by MoS_3 and MoS_2 particles. *Energy Environ. Sci.* **5**, 6136–6144 (2012).
43. A. J. Bard, L. R. Faulkner, Chapter 10: Techniques based on concepts of impedances, in *Electrochemical Methods: Fundamentals and Applications* (Wiley, New York, 1980), pp. 368–416.
44. E. Barsoukov, J. R. Macdonald, Chapter 2: Theory, in *Impedance Spectroscopy: Theory, Experiment, and Applications* (Wiley, Hoboken, NJ, 2005), pp. 27–128.
45. S. Trasatti, O. Petrii, Real surface area measurements in electrochemistry. *Pure Appl. Chem.* **63**, 711–734 (1991).
46. J. D. Benck, Z. Chen, L. Y. Kuritzky, A. J. Forman, T. F. Jaramillo, Amorphous molybdenum sulfide catalysts for electrochemical hydrogen production: Insights into the origin of their catalytic activity. *ACS Catal.* **2**, 1916–1923 (2012).
47. J. Bonde, P. G. Moses, T. F. Jaramillo, J. K. Nørskov, I. Chorkendorff, Hydrogen evolution on nano-particulate transition metal sulfides. *Faraday Discuss.* **140**, 219–231 (2009).
48. H. Topsøe, B. S. Clausen, R. Candia, C. Wivel, S. Mørup, In situ Mössbauer emission spectroscopy studies of unsupported and supported sulfided Co-Mo hydrodesulfurization catalysts: Evidence for and nature of a Co-Mo-S phase. *J. Catal.* **68**, 433–452 (1981).
49. J. Lauritsen, S. Helveg, E. Lægsgaard, I. Stensgaard, B. Clausen, H. Topsøe, F. Besenbacher, Atomic-scale structure of Co-Mo-S nanoclusters in hydrotreating catalysts. *J. Catal.* **197**, 1–5 (2001).
50. J. V. Lauritsen, J. Kibsgaard, G. H. Olesen, P. G. Moses, B. Hinnemann, S. Helveg, J. K. Nørskov, B. S. Clausen, H. Topsøe, E. Lægsgaard, F. Besenbacher, Location and coordination of promoter atoms in Co- and Ni-promoted MoS_2-based hydrotreating catalysts. *J. Catal.* **249**, 220–233 (2007).
51. L. S. Byskov, B. Hammer, J. K. Nørskov, B. Clausen, H. Topsøe, Sulfur bonding in MoS_2 and Co-Mo-S structures. *Catal. Lett.* **47**, 177–182 (1997).
52. J. H. Espenson, Chapter 1: Reaction and reaction rates, in *Chemical Kinetics and Reaction Mechanisms* (McGraw, New York, NY, 2002), pp. 1–14.
53. M. A. Lukowski, A. S. Daniel, F. Meng, A. Forticaux, L. Li, S. Jin, Enhanced hydrogen evolution catalysis from chemically exfoliated metallic MoS_2 nanosheets. *J. Am. Chem. Soc.* **135**, 10274–10277 (2013).
54. U. Muller, Chapter 16: Linked polyhedra, in *Inorganic Structural Chemistry* (Wiley, Chichester, UK, ed. 2, 2007), pp. 166–189.
55. Q. He, X. Yang, W. Chen, S. Mukerjee, B. Koel, S. Chen, Influence of phosphate anion adsorption on the kinetics of oxygen electroreduction on low index Pt(*hkl*) single crystals. *Phys. Chem. Chem. Phys.* **12**, 12544–12555 (2010).

56. S. M. A. M. Bouwens, J. P. R. Vissers, V. H. J. de Beer, R. Prins, Phosphorus poisoning of molybdenum sulfide hydrodesulfurization catalysts supported on carbon and alumina. *J. Catal.* **112**, 401–410 (1988).
57. L. Qingfeng, H. A. Hjuler, N. J. Bjerrum, Oxygen reduction on carbon supported platinum catalysts in high temperature polymer electrolytes. *Electrochim. Acta* **45**, 4219–4226 (2000).
58. P.-C. Chen, Y.-M. Chang, P.-W. Wu, Y.-F. Chiu, Fabrication of Ni nanowires for hydrogen evolution reaction in a neutral electrolyte. *Int. J. Hydrogen Energy* **34**, 6596–6602 (2009).
59. F. Harnisch, G. Sievers, U. Schröder, Tungsten carbide as electrocatalyst for the hydrogen evolution reaction in pH neutral electrolyte solutions. *Appl. Catal. B: Environ.* **89**, 455–458 (2009).
60. C. He, X. Wu, Z. He, Amorphous nickel-based thin film as a Janus electrocatalyst for water splitting. *J. Phys. Chem. C* **118**, 4578–4584 (2014).
61. S. Cobo, J. Heidkamp, P.-A. Jacques, J. Fize, V. Fourmond, L. Guetaz, B. Jousselme, V. Ivanova, H. Dau, S. Palacin, M. Fontecave, V. Artero, A Janus cobalt-based catalytic material for electro-splitting of water. *Nat. Mater.* **11**, 802–807 (2012).
62. W. Cui, Q. Liu, Z. Xing, A. M. Asiri, K. A. Alamry, X. Sun, MoP nanosheets supported on biomass-derived carbon flake: One-step facile preparation and application as a novel high-active electrocatalyst toward hydrogen evolution reaction. *Appl. Catal. B: Environ.* **164**, 144–150 (2015).
63. J. F. Callejas, J. M. McEnaney, C. G. Read, J. C. Crompton, A. J. Biacchi, E. J. Popczun, T. R. Gordon, N. S. Lewis, R. E. Schaak, Electrocatalytic and photocatalytic hydrogen production from acidic and neutral-pH aqueous solutions using iron phosphide nanoparticles. *ACS Nano* **8**, 11101–11107 (2014).
64. N. Jiang, L. Bogoev, M. Popova, S. Gul, J. Yano, Y. Sun, Electrodeposited nickel-sulfide films as competent hydrogen evolution catalysts in neutral water. *J. Mater. Chem. A* **2**, 19407–19414 (2014).
65. S. Gupta, N. Patel, A. Miotello, D. C. Kothari, Cobalt-boride: An efficient and robust electrocatalyst for hydrogen evolution reaction. *J. Power Sources* **279**, 620–625 (2015).
66. D. Merki, S. Fierro, H. Vrubel, X. Hu, Amorphous molybdenum sulfide films as catalysts for electrochemical hydrogen production in water. *Chem. Sci.* **2**, 1262–1267 (2011).
67. J. Kim, S. Byun, A. J. Smith, J. Yu, J. Huang, Enhanced electrocatalytic properties of transition-metal dichalcogenides sheets by spontaneous gold nanoparticle decoration. *J. Phys. Chem. Lett.* **4**, 1227–1232 (2013).
68. Y. Tan, P. Liu, L. Chen, W. Cong, Y. Ito, J. Han, X. Guo, Z. Tang, T. Fujita, A. Hirata, M. W. Chen, Monolayer MoS_2 films supported by 3D nanoporous metals for high-efficiency electrocatalytic hydrogen production. *Adv. Mater.* **26**, 8023–8028 (2014).

Funding: This work was supported by Nanyang Technological University (M4080977.120.50000), Singapore Ministry of Education under Academic Research Fund (AcRF) Tier 2 (ARC 26/13, no. MOE2013-T2-1-034; ARC 19/15, no. MOE2014-T2-2-093), AcRF Tier 1 (RG 9/12, RG 61/12, RGT18/13, and RG5/13), and Start-Up grant (M4081296.070.500000). This research is also conducted by Nanyang Technological University–Hebrew University of Jerusalem–Ben-Gurion University Nanomaterials for Energy and Water Management Programme under the Campus for Research Excellence and Technological Enterprise, which is supported by the National Research Foundation, Prime Minister's Office, Singapore. **Author contributions:** B.L. and H.Z. conceived the idea and supervised the research work. J.M. designed the experiments and fabricated the electrodes. J.M. conducted the SEM and XRD experiments. F.-X.X. carried out the XPS measurements. H.B.Y. conducted the TEM and Raman spectroscopy experiments. S.Y.K. analyzed the EIS data and performed molecular mechanical simulation. Y.-Y.H. and H.M.C. carried out and analyzed the EXAFS experiments. B.L. and J.M. wrote the manuscript with critical inputs from J.C., Z.F., and H.Z. **Competing interests:** The authors declare that they have no competing interests.

Submitted 27 February 2015
Accepted 16 July 2015
Published 21 August 2015
10.1126/sciadv.1500259

Citation: J. Miao, F.-X. Xiao, H. B. Yang, S. Y. Khoo, J. Chen, Z. Fan, Y.-Y. Hsu, H. M. Chen, H. Zhang, B. Liu, Hierarchical Ni-Mo-S nanosheets on carbon fiber cloth: A flexible electrode for efficient hydrogen generation in neutral electrolyte. *Sci. Adv.* **1**, e1500259 (2015).